# Plasticity of cell migration resulting from mechanochemical coupling

**Yuansheng Cao**[1†]**, Elisabeth Ghabache**[1†]**, Wouter-Jan Rappel**[1]

**\*For correspondence:**
rappel@physics.ucsd.edu (WJR)

[†]These authors contributed equally to this work

[1]Department of Physics, University of California, San Diego, La Jolla, California 92093, USA

**Abstract**   Eukaryotic cells can migrate using different modes, ranging from amoeboid-like, during which actin filled protrusions come and go, to keratocyte-like, characterized by a stable morphology and persistent motion. How cells can switch between these modes is not well understood but waves of signaling events are thought to play an important role in these transitions. Here we present a simple two-component biochemical reaction-diffusion model based on relaxation oscillators and couple this to a model for the mechanics of cell deformations. Different migration modes, including amoeboid-like and keratocyte-like, naturally emerge through transitions determined by interactions between biochemical traveling waves, cell mechanics and morphology. The model predictions are explicitly verified by systematically reducing the protrusive force of the actin network in experiments using *Dictyostelium discoideum* cells. Our results indicate the importance of coupling signaling events to cell mechanics and morphology and may be applicable in a wide variety of cell motility systems.

## Introduction

Eukaryotic cell migration is a fundamental biological process that is essential in development and wound healing and plays a critical role in pathological diseases, including inflammation and cancer metastasis *Ridley et al.* (*2003*); *Roussos et al.* (*2011*); *Montell* (*2003*). Cells can migrate using a variety of modes with a range of corresponding morphologies. The repeated extensions and retractions of pseudopods in amoeboid-like cells, for example, result in a constantly changing morphology and random migration while keratocyte-like cells have a stable and broad actin-rich front, a near-constant shape, and move in a persistent fashion *Webb and Horwitz* (*2003*); *Keren et al.* (*2008*). Furthermore, many cells do not have a unique migration mode and can switch between them, either as a function of the extracellular environment or upon the introduction of a stimulus *Paul et al.* (*2017*); *Bergert et al.* (*2012*); *Charras and Sahai* (*2014*); *Liu et al.* (*2015*); *Petrie and Yamada* (*2016*); *Miao et al.* (*2017*). This plasticity is currently poorly understood and is thought to play a role in pathological and physiological processes that involve cell migration, including cancer metastasis *Friedl and Alexander* (*2011*).

A key step in cell migration is the establishment of an asymmetric and polarized intra-cellular organization where distinct subsets of signaling molecules, including PAR proteins, Rho family GTPases and phosphoinositides, become localized at the front or back of the cell *Jilkine and Edelstein-Keshet* (*2011*); *Rameh and Cantley* (*1999*); *Goldstein and Macara* (*2007*); *Raftopoulou and Hall* (*2004*); *Rappel and Edelstein-Keshet* (*2017*). In the absence of directional cues, this symmetry breaking can be a spontaneous and dynamic process with waves of cytoskeletal and signaling components present on the cell cortex *Vicker* (*2002*); *Weiner et al.* (*2007*); *Whitelam et al.* (*2009*); *Case and Waterman* (*2011*); *Gerisch et al.* (*2012*); *Allard and Mogilner* (*2013*); *Gerhardt et al.* (*2014*); *Barnhart et al.* (*2017*). Addressing this spontaneous symmetry breaking and the role of waves have generated numerous theoretical studies *Jilkine and Edelstein-Keshet* (*2011*); *Meinhardt* (*1999*); *Ot-*

suji et al. (*2007*); *Csikász-Nagy et al.* (*2008*); *Beta et al.* (*2008*); *Mori et al.* (*2008*); *Xiong et al.* (*2010*); *Knoch et al.* (*2014*); *Miao et al.* (*2017*). Most models, however, study cell polarity in the context of biochemical signaling and do not consider cell movement or deformations originated from cell mechanics. This may be relevant for nonmotile cells including yeast *Park and Bi* (*2007*); *Slaughter et al.* (*2009*) but might not be appropriate for motile cells where the coupling between intracellular pathways and cell shape can be crucial in determining the mode of migration*Camley et al.* (*2013*, 2017). Furthermore, most of these models only focus on one specific migration mode and do not address transitions between them. Therefore, it remains an open question how cell mechanics, coupled to a biochemical signaling module, can affect spontaneous cell polarity and can determine transitions between cell migration modes.

Here we propose a novel model that couples an oscillatory biochemical module to cell mechanics. Our choice of the biochemical model was motivated by recent findings that the self-organized phosphatidylinositol (PtdIns) phosphate waves on the membrane of Dictyostelium cells exhibit characteristics of a relaxation oscillator *Arai et al.* (*2010*). Our model is able to generate amoeboid-like, keratocyte-like, and oscillatory motion by varying a single mechanical parameter, the protrusive strength, without altering the biochemical signaling pathway. We determine how the transitions depend on these parameters and we show that keratocyte-like motion is driven by an emergent traveling wave whose stability is determined by the mechanical properties of the cell. Finally, we experimentally obtain all three migration modes in wild-type *Dictyostelium discoideum* and explicitly verify model predictions by reducing the actin protrusive force using the drug latrunculin B. Our model provides a unified framework to understand the relationship between cell polarity, motility and morphology determined by cellular signaling and mechanics.

## Models and results

### Model

Our two-dimensional model is composed of two modules: a biochemical module describing the dynamics of an activator-inhibitor system which works in the relaxation oscillation regime, and a mechanical module that describes the forces responsible for cell motion and shape changes (Fig.1a). Our biochemical module consists of a reaction-diffusion system with an activator $A$ (which can be thought of as PtdIns phosphates and thus upstream from newly-polymerized actin *Gerhardt et al.* (*2014*); *Miao et al.* (*2019*)) and an inhibitor $R$ (which can be thought of as the phosphatase PTEN). This activator and inhibitor diffuse in the cell and obey equations that reproduce the characteristic relaxation oscillation dynamics in the PtdIns lipid system *Arai et al.* (*2010*); *Matsuoka and Ueda* (*2018*); *Fukushima et al.* (*2018*):

$$\frac{\partial A}{\partial t} = D_A \nabla \cdot (\nabla A) + F(A) - G(R)A + \zeta_1(t),$$  (1)

$$\frac{\partial R}{\partial t} = D_R \nabla \cdot (\nabla R) + \frac{c_2 A - c_1 R}{\tau} + \zeta_2(t),$$  (2)

where $D_A$ and $D_R$ are the diffusion coefficients for $A$ and $R$, respectively. In these expressions, $F(A)$ is the self-activation of the activator with a functional form that is similar to previous studies: $F(A) = [k_a A^2/(K_a^2 + A^2) + b](A_t - A)$ *Miao et al.* (*2017*). The activator is inhibited by $R$ through the negative feedback $G(R) = d_1 + d_2 R$ while $R$ is linearly activated by $A$ (see Methods and Materials). The timescale of the inhibitor $\tau$ is taken to be much larger than the timescale of the activator, set by $k_a$: $\tau \gg k_a^{-1}$. Finally, to ensure robustness to stochasticity, we add uniformly distributed spatial white noise terms $\langle \zeta_i(\mathbf{r}, t)\zeta_j(\mathbf{r}', t')\rangle = \sigma \delta_{ij}\delta(\mathbf{r} - \mathbf{r}')\delta(t - t')$.

Nullclines for this system are shown in Fig.1b, where we have chosen parameters such that the fixed point is unstable and the system operates in the oscillatory regime. As a result of the separation of timescales for $A$ and $R$, the dynamics of $A$ and $R$ are characteristic of a relaxation oscillator (inset of Fig.1b): $A$ reaches its maximum quickly, followed by a slower relaxation phase during which the system completes the entire oscillation period.

79　　To generate cell motion, we couple the output of the biochemical model to a mechanical module
80　which incorporates membrane tension and protrusive forces that are proportional to the levels of
81　activator $A$ and normal to the membrane, similar to previous studies *Shao et al.* (*2010*, 2012) (see
82　Methods and Fig.1a). To accurately capture the deformation of the cell in simulations, we use the
83　phase field method *Shao et al.* (*2010*); *Ziebert et al.* (*2011*); *Shao et al.* (*2012*); *Najem and Grant*
84　(*2013*); *Marth and Voigt* (*2014*); *Camley et al.* (*2017*); *Cao et al.* (*2019*). Here, an auxiliary field $\phi$ is
85　introduced to distinguish between the cell interior ($\phi = 1$) and exterior ($\phi = 0$), and the membrane
86　can be efficiently tracked by the contour $\phi = 1/2$. Coupling this field to the reaction-diffusion
87　equations can guarantee that no-flux boundary conditions at the membrane are automatically
88　satisfied *Kockelkoren et al.* (*2003*). The evolution of the phase-field is then determined by the force
89　balance equation:

$$\xi\frac{\partial \phi}{\partial t} = \eta M(A)|\nabla \phi| - \frac{\delta H(\phi)}{\epsilon \delta \phi}, \tag{3}$$

90　where $\xi$ is a friction coefficient, $\epsilon$ is the boundary width of the phase field, and $H(\phi)$ is a Hamil-
91　tonian energy including the membrane tension, parameterized by $\gamma$ and area conservation (see
92　Methods and Materials). The first term on the right hand side describes the actin protrusive force,
93　parameterized by $\eta$, and acts on the cell boundary since $|\nabla\phi|$ is non-zero only in a region with width
94　$\epsilon$. $M$ formulates the dependence of the protrusive force on the activator levels and is taken to be
95　sigmoidal: $M(A) = A^n/(A^n + A_0^n)$, where $n$ is a Hill coefficient. As initial conditions, we use a disk with
96　radius $r$ with area $S = \pi r^2$ and set $A = R = 0$. Default parameter values for our model are estimated
97　from experimental data and given in Table 1.

98　　Cell motion is quantified by computing the velocity of the center of mass of the cell. Furthermore,
99　we record the trajectory of the center of mass and compute its average curvature $\langle \kappa \rangle = \int \kappa(l)dl/L$,
100　where $k(l)$ is the local curvature, and $L$ is the total length of the trajectory. These quantities can be
101　used to distinguish between different migration modes (see Results and Methods and Materials).

## Computational results

103　We first examine the possible migration modes as a function of the protrusive strength $\eta$ for fixed
104　area $S$, parametrized by the radius $r$ of the disk used as initial condition, and default parameters.
105　As shown in Fig.2, there are three distinct cell migration modes. When $\eta$ is small, activator waves
106　initiate in the interior and propagate to the cell boundary. However, the protrusive force is too
107　small to cause significant membrane displacement, as also can be seen from the trajectory in Fig.2b.
108　Consequently, the cell is almost non-motile and the activator and inhibitor field show oscillatory
109　behavior (Fig.2a I &b and Video 1).

110　　As $\eta$ increases, an activator wave that reaches the boundary can create membrane deformations,
111　leading to the breaking of spatial homogeneity. This wave, however, is competing with other
112　traveling waves that emerge from random positions. Consequently, the cell exhibits transient
113　polarity, moves in constantly changing directions, and displays amoeboid-like migration (Fig.2a II &b
114　and Video 2).

115　　When $\eta$ is increased further, protrusions generated by activator waves reaching the cell boundary
116　become even larger. As a result of the coupling between the waves and membrane mechanics, a
117　single traveling wave will emerge within the cell, characterized by a broad and stationary band of
118　high levels of activator. This wave pushes the membrane forward in a persistent direction with
119　constant speed and the cell will adopt a steady keratocyte-like morphology, even in the presence of
120　noise (Fig.2a III &b and Video 3).

121　　The transition from oscillatory dynamics to amoeboid-like unstable cell motion can be under-
122　stood by considering the coupling between the traveling waves and membrane motion. In Methods
123　and Materials we show that these traveling waves, that emerge naturally in systems of relaxation
124　oscillators *Kopell and Howard* (*1973*); *Keener* (*1980*); *Murray* (*2002*) are stable as long as the acti-
125　vator front can "outrun" the inhibitor's spreading speed. This condition results in a minimal wave
126　speed $c_{\min}$ that depends on $D_R$ and $\tau$ (see Methods and Materials ). The activator wave pushes

127 the membrane outward and will keep propagating as long as the boundary can keep up with the
128 wave speed. In our model, the membrane is pushed outward by a protrusive force resulting in
129 a speed approximately given by $v_b \sim \alpha\eta/\xi$, where $\alpha$ is the boundary-averaged value of $M(A)$, that
130 depends on mechanical parameters and is independent of biochemical parameters (see Methods
131 and Materials and Fig2–Figure Supplement 1). This implies that if the speed of the membrane is
132 less that the minimum speed of the activator wave ($v_b < c_{\min}$) there will be no significant membrane
133 motion. On the other hand, when $v_b > c_{\min}$, a traveling wave can be selected by matching the wave
134 speed and the boundary speed:

$$c = v_b \sim \frac{\alpha\eta}{\xi}. \tag{4}$$

135 The above equation indicates that when $\eta > \xi c_{\min}/\alpha$, the cell will break its symmetric shape through
136 traveling waves that deform the membrane.

137 In simulations, the critical value of $\eta$, $\eta_{c,1}$, for which the oscillating cell becomes amoeboid-like
138 can be determined by slowly increasing $\eta$ and computing the center-of-mass speed of the cell,
139 $v_{CM}$. Oscillatory cells are then defined as cells with a vanishing center of mass speed (see also
140 Methods and Materials). The transition between oscillatory and amoeboid-like cells is shown in
141 Fig.2c where we plot $v_{CM}$ as a function of protrusion strength $\eta$ for cells with as initial condition
142 either homogeneous solutions in $A$ and $R$ that are perturbed with noise (blue curve) or asymmetric
143 distributions of $A$ and $R$ (red curve). For both initial conditions, the speed shows a subcritical
144 bifurcation at a critical value of $\eta_{c,1}$, above which a non-zero cell speed emerges. Furthermore, these
145 simulations reveal that, as argued above, $\eta_{c,1}$ depends on both $D_R$ and $\tau$ (Fig2– Figure Supplement
146 2).

147 Once a traveling wave is able to generate membrane deformations, why does it not always
148 result in stable, keratocyte-like motion with a single traveling wave in the cell's interior? Notice
149 that in our model, if the spatial extent between the cell front and the back, $d$, is larger than the
150 wavelength of the activator wave $\lambda$ (schematically shown in Fig.1a), a new wave will be generated
151 behind the original one. This wavelength can be approximated by $\lambda \approx \sqrt{2D\tau}$ (where we have
152 taken $D_A = D_R = D$ for simplicity) such that stable keratocyte-like cells driven by a single wave are
153 only possible when $d < \lambda$. This front-back distance, however, depends on the balance between
154 protrusive force and membrane tension at the traveling wave's lateral ends. Increasing values
155 of $\eta$ result in a broader front and therefore smaller values of $d$ (Fig.2 d). As a consequence, as
156 $\eta$ is increased, waves propagating within the cell eventually become stable, resulting in a single,
157 propagating wave and a cell with a keratocyte-like morphology. For a discussion on the role of
158 tension we refer to Methods and Materials and Fig2– Figure Supplement 3.

159 To distinguish between keratocyte-like and amoeboid-like cells we compute the average cur-
160 vature of the center of mass trajectory $\langle\kappa\rangle$ (see Methods and Materials). For keratocyte-like cells,
161 which move in a more persistent way, $\langle\kappa\rangle$ will take on small values while for amoeboid-like cells $\langle\kappa\rangle$
162 will become large. This is shown in Fig. 2e where we plot $\langle\kappa\rangle$ as a function of protrusion strength
163 (red curve). The transition from unstable to stable polarity, and therefore keratocyte-like motion,
164 happens smoothly in a narrow region of $\eta$ and the critical value $\eta_{c,2}$ can be defined as the point
165 for which $\langle\kappa\rangle = 0.02\mu m^{-1}$. Alternatively, and as in the experiments, we can compute the standard
166 deviation of angles of trajectory points, taken at fixed intervals (see Methods and Materials). As illus-
167 trated by the blue curve in Fig. 2e, this standard deviation also decreases rapidly as $\eta$ is increased
168 and thus provides an alternative method to distinguish the two cell migration modes.

169 Our analysis also implies that for equal protrusive strengths larger cells will be less stable. These
170 cells have a larger area which allows for the nucleation of a new wave front which destabilizes the
171 cell. For equal size cells, those with a smaller protrusion strength would have a larger font-back
172 distance (Fig. 2d) and therefore more space to generate a new wave, potentially destabilizing them.
173 Consequently, decreasing the protrusion would destabilize larger keratocyte-like cells and only
174 smaller keratocyte-like cells will remain.

175 From the above analysis, it becomes clear that the protrusive strength and size of initial disk,

176 and thus cell area, are critical parameters in determining the stability of the polarity established
177 by interactions between traveling waves and moving boundaries. In simulations, we therefore
178 determine the phase diagram in the $(\eta, S)$ space by systematically varying the initial radius (with
179 step size 0.5 $\mu$m) and protrusive force (with step size 0.25 pN) while keeping all other parameters
180 fixed (Fig.2 f). We constrain our cell area to be within the physiologically relevant range with a
181 initial radius between $r = 4\mu$m and $r = 8\mu$m, corresponding to an area between $S \sim 50\mu$m$^2$ and
182 $S \sim 200\mu$m$^2$ (see Methods and Materials and Fig2–Figure Supplement 4 for an extension of the
183 phase space to larger values of $r$). As stated above, there are three distinct phases, corresponding to
184 the three different cell migration modes of Fig.2a. The transition from oscillatory to amoeboid-like
185 motility occurs at small $\eta$ and is independent of cell size, as predicted in Eq.(4). The transition from
186 unstable to stable polarity is quantified by $\eta_{c,2}$, which increases for increasing values of $r$ and thus $S$.
187 The latter transition depends on parameters that affect either $d$ or $\lambda$ (Fig.2 g). For example, we
188 can reduce the timescale of the inhibitor $\tau$ to half the value reported in Table S1 ($\tau_0$) which leads
189 to a decrease of $\lambda$ and should lead to larger values of $\eta_{c,2}$. Secondly, for increasing values of the
190 membrane tension the transition occurs for larger values of $\eta$. This can be understood by realizing
191 that an increase in the membrane tension will reduce the cell's deformability. Therefore, the
192 curvature of the cell's front will decrease, which will increase the front-back distance and thus the
193 critical protrusion strength. Finally, increasing value of the friction coefficient $\xi$ should, according to
194 Eq.4, lead to a decrease in the membrane speed. Since the biochemical wave speed $c$ is unchanged,
195 the transition from amoeboid-like to keratocyte-like motion should occur for larger values of $\eta$. All
196 those predictions are confirmed in our simulations, as shown in Fig.2 g. Importantly, we find the
197 speed of the keratocyte-like cell in all the situations is linearly dependent on $\eta/\xi$, and independent
198 of other parameters, as predicted by Eq. 4 (Fig.2 h).
199 In summary, our model predicts that a sufficient decrease of $\eta$ can destabilize keratocyte-like
200 cells, resulting in cells that employ amoeboid-like migration, and can transform keratocyte-like and
201 unstable cells into oscillatory cells. Furthermore, for decreasing protrusive force, the keratocyte-like
202 cells should have a reduced speed and cell size.

## Experimental Results

204 To test our model predictions, we carry out experiments using wild-type Dictyostelium cells (see
205 Methods and Materials). In vegetative food-rich conditions, during which food is plentiful, most
206 cells migrate randomly using amoeboid-like motion. Starvation triggers cell-cell signaling after
207 which cells become elongated and perform chemotaxis. However, we found that starving cells for
208 6h at sufficiently low density is enough to prevent cell-cell signaling. Under these conditions, the
209 majority of cells still moves as amoeboid-like cells but a significant fraction, approximately 20-50%,
210 migrates in a keratocyte-like fashion (Video 4). These cells adopt a fan-shaped morphology and
211 move unidirectionally, as was also observed in certain Dictyostelium mutants *Asano et al.* (*2004*).
212 Employing these low density conditions, we can alter the cell's protrusive force by interrupting actin
213 polymerization using the drug latrunculin B, an inhibitor of actin activity. Our model predicts that as
214 the concentration of latrunculin increases, keratocyte-like cells are more likely to switch to unstable
215 or oscillatory cells. Furthermore, the size and speed of the remaining keratocyte-like cells should
216 decrease.
217 A snapshot of starved cells is shown in Fig. 3a, before (left panel) and after exposure to
218 latrunculin (right panel). Higher magnification plots of the amoeboid-like cells (top two panels) and
219 of a keratocyte-like cell are shown to the right. In these panels, the actin distribution is visualized
220 with the fluorescent marker limE-GFP. As can be seen by comparing the snapshots in Fig. 3a, the
221 number of keratocyte-like cells decreases after the exposure of latrunculin. This decrease is due
222 to keratocyte-like cells becoming unstable and switching to the amoeboid-like mode of migration.
223 We quantify the percentage of keratocyte-like cells, as well as the speed and shape, as a function
224 of time for different concentrations of latrunculin for at least 100 cells. As shown in Fig. 3b, the
225 percentage of keratocyte-like cells decreases upon the introduction of latrunculin. Furthermore,

226 this decrease becomes more pronounced as the concentration of latrunculin is increased (inset Fig.
227 3b), consistent with our model prediction.

228 To further verify the model predictions, we quantify the cell area $S$ and cell speed for the
229 keratocyte-like cells. Both the area (fig.3c) and speed (fig.3d) decrease after the introduction of
230 latrunculin. This decrease becomes more significant for larger concentrations of latrunculin, again
231 consistent with our predictions. The effect of latrunculin is further shown in Fig3–Figure Supplement
232 1 where we plot the speed of the amoeboid and keratocyte-like cells for different areas as a function
233 of latrunculin concentration. Speed decreases for increasing latrunculin concentration, indicating
234 that the protrusive force is reduced in the presence of latrunculin.

235 Finally, our model predicts that, with a relaxed area conservation, a sufficient reduction of
236 protrusive strength results in the appearance of oscillatory cells with oscillating basal area size
237 (Fig2–Figure Supplement 5). Indeed, after the exposure to latrunculin, a small fraction of cells
238 are observed to display oscillatory behavior characterized by repeated cycle of spreading and
239 contraction, resulting in a basal surface area that oscillates, similar to the engineered oscillatory
240 cells of *Miao et al.* (*2017*) (Fig. 3e). Cell tracking reveals that these cells originate through a transition
241 from the unstable, amoeboid-like state to the oscillatory state. Interestingly, the observed oscillation
242 in surface area is often very regular (Fig. 3e). We find that the average period of different cells is
243 largely independent of the latrunculin concentration, ranging from 6.2 ± 0.9 min for 1 $\mu$M to 6.6 ±
244 0.9 min for 4 $\mu$M, while the coefficient of variation, defined as the ratio of the standard deviation
245 and the mean, for single cell periods varies between 0.31 ± 0.12 min (1 $\mu$M) and 0.20 ± 0.10 min (4
246 $\mu$M; Fig3–Figure Supplement 2).

247 Our experimental results can be summarized by identifying the migration mode of cells for
248 different values of the cell area and the latrunculin concentration, thus constructing a phase diagram
249 that can be compared to the computational one (Fig. 2f). Due to cell-to-cell variability, we find a
250 distribution of migration modes for each point in this phase diagram. This is shown in Fig. 3f where
251 we plot, using a separate color scale for each migration mode, the percentage of keratocyte-like,
252 amoeboid-like, and oscillatory mode of migration for different values of the cell area and latrunculin
253 concentration. The resulting experimental phase diagrams agree well with the computational phase
254 diagram presented in Fig. 2f. Without latrunculin, many cells migrate using the keratocyte-like
255 mode. Exposing cells to latrunculin, and thus reducing the protrusive force, results in a shift from
256 keratocyte-like towards amoeboid-like cells. Furthermore, for the maximum value of the latrunculin
257 concentration, almost all keratocyte-like cells are destabilized and a small proportion of cells ($\approx$ 9%)
258 are in the oscillatory mode. Thus, our experimental results are in good agreement with the model
259 predictions.

## Discussion

261 In this paper, we propose a simple but unified paradigm to understand cell migration and cell
262 morphology. As in previous modeling studies *Nishimura et al.* (*2009*, 2012); *Miao et al.* (*2017*,
263 2019), our model displays different migration modes. These modes can be induced by varying the
264 protrusive force which is attractive since the switching of these modes can occur on a timescale that
265 is shorter than gene expression timescales (Fig. 3b), suggesting that a single model with conserved
266 components should be able to capture all three modes. Importantly, our model predictions are
267 verified in experiments using wild-type Dictyostelium cells which, under our conditions, exhibit all
268 three migration modes. These experiments show that upon the introduction of latrunculin the
269 speed of keratocyte-like cells decrease. This is perhaps not surprising since latrunculin inhibits actin
270 polymerization which can be expected to result in smaller cell speeds. Our experiments also show,
271 however, that the area of the moving keratocyte-like cells decreases in the presence of latrunculin.
272 In addition, and more importantly, our experiments demonstrate that transitions between the
273 migration modes can be brought about by reducing the protrusive strength of the actin network.
274 These non-trivial effects of latrunculin are consistent with the predictions of our model and are also
275 captured in our experimental phase diagrams (Fig. 3f).

Key in our model is the coupling of traveling waves generated through biochemical signaling and cell mechanics. Our main finding is that cell migration is driven by the traveling waves and that persistent propagation of these waves result in keratocyte-like cells with a broad and stable front. This stable front is only present if the front-back distance is smaller than the biochemical wavelength. Reducing the protrusive strength results in a larger front-back distance, resulting in unstable, amoeboid-like migration. For even smaller values of the protrusive strength, cells display oscillatory behavior. For these values, the membrane speed is smaller than the minimum biochemical wave speed.

Several recent computational studies have addressed switching between different migration modes. For example, Nishimura et al. have presented a model that includes actin and cortical factors, control factors of actin polymerization, and have shown that feedback between cell shape deformations and the spatially distributed control factors can result in amoeboid-like motion *Nishimura et al.* (*2009*, 2012) . Furthermore, changing the rate of polymerization as well as the threshold of polymerization in the model can result in transitions between amoeboid-like and keratocyte-like cells *Nishimura et al.* (*2009*, 2012). In addition, Miao et al. have proposed a model that can generate all three migration modes observed in experiments of engineered Dictyostelium cells *Miao et al.* (*2017*, 2019). This model contains an excitable network and the different migration modes can be generated by altering the threshold of this network. Our current model is distinct from these studies in several ways. First, the migration mode transitions in our model are induced by the mechanical module with the same biochemical components, while in other models the transitions are generated by changing the dynamics of the biochemical signaling pathways from, e.g., excitable to oscillatory *Miao et al.* (*2017*), or the threshold of actin polymerization *Nishimura et al.* (*2009*, 2012). In addition, the biochemical module in our model is much simpler and only contains an activator and inhibitor while the model of *Miao et al.* (*2017*) requires additional feedback from a postulated polarity module. Of course, our work does not exclude the existence of this polarity module but it shows that we can explain the observed cell morphologies and movement within a minimal framework of coupling two biochemical components and cell mechanics. Second, based on the earlier measurements of *Arai et al.* (*2010*), our model assumes that the biochemical module operates as a relaxation oscillator. As a result, and in contrast to *Nishimura et al.* (*2009*, 2012), our model is able to generate oscillatory cells. This is also in contrast to the model of *Miao et al.* (*2017*), which uses nested excitable networks. Note however, that in our model we can tune the negative feedback to make the biochemical module operate in the excitable regime. We have explicitly verified that qualitatively similar migration modes and transitions are observed if our model is excitable (Fig2–Figure Supplement 6). In the excitable version of our model, however, the oscillations in the non-motile mode are, in general, less regular and periodic than the ones obtained in the relaxation oscillator version. From the statistical features of the periods obtained from oscillatory cells in experiments, it is likely that the cellular signaling dynamics can be most accurately described by relaxation oscillation models. As a final distinction, we point out that the biochemical and mechanical module in the model of *Miao et al.* (*2017*) are solved separately on a 1D ring while in *Nishimura et al.* (*2009*, 2012), the biochemical reactions are coupled to cell deformation in a lattice model. As a result, the keratocyte-like cells in *Miao et al.* (*2017*) display constant excitations at the front that travel along the membrane in the lateral direction rather than stationary activator bands, as observed in the experiments and in our model (Fig.3a(v)). Furthermore, the keratotyte-like cells in *Nishimura et al.* (*2009*, 2012) have similar shape to the ones generated in our model but have less persistent directionality.

Several future extensions of our study are possible. First, our current study is restricted to two dimensional geometries while actual cell motion is of course three dimensional. Extending our model to 3D would allow us to relax the area conservation constraint and should result in cells for which the basal surface area show clear oscillations that are coupled to extensions away from the surface (Fig2–Figure Supplement 5). Second, we have ignored fluid flow within the cytosol, which may play a role in signaling and polarity formation. Including fluid flow, which adds considerable

327 computational complexity to the model *Shao et al.* (*2012*), will be part of future extensions. Third, it
328 should be possible to couple the biochemical model to upstream chemotaxis pathways, allowing it
329 to address directed motion or more complex pathways. In addition, it should be possible to consider
330 multiple parallel and excitable pathways which may regulate cell motility in chemotaxis *Tanabe*
331 *et al.* (*2018*) and models with more molecular details *Matsuoka and Ueda* (*2018*); *Fukushima*
332 *et al.* (*2018*). Fourth, it would be interesting to compare wave dynamics obtained in our model
333 with waves observed in giant Dictyostelium cells *Gerhardt et al.* (*2014*). In addition, alternative
334 biochemical models in which parameters determine the qualitatively different dynamics can be
335 studied *Miao et al.* (*2017*). Furthermore, our study predictions may also be verified in other cell
336 types. For example, we predict that overexpression of actin in fast moving cells should result in cells
337 migrating with keratocyte-like morphologies while disturbing actin polymerization in keratocytes
338 could lead to unstable migration. Finally, it would be interesting to determine how the feedback
339 between mechanical and biochemical modules can potentially help understand other cell migration
340 processes.

## Acknowledgments

## Methods and Materials

### Full model

346 Our model for the cell boundary and cell motion is detailed in earlier studies *Shao et al.* (*2010*,
347 2012); *Camley et al.* (*2014*). Briefly, we model the cell boundary as an interface with tension, driven
348 in this study by activator $A$ at the front. Cell motion obeys the overdamped force balance equation
349 $F_{act} + F_{mem} + F_{area} + F_{fric} = 0$ where $F_{act}$ is the active force proportional to the activator concentration;
350 $F_{mem}$ describes the membrane tension (line tension since we are modeling a 2D cell); $F_{area}$ represents
351 area conservation to prevent cells from expanding or shrinking indefinitely and $F_{fric}$ is a friction
352 force. The active force from the activator is governed by $F_{act} = \eta M(A)\hat{n}$, where $\hat{n} = -\nabla\phi/|\nabla\phi|$ is the
353 outward-pointing normal direction of the membrane, and $M(A) = A^3/(A^3 + A_0^3)$ where $A_0$ represents
354 a threshold value for activation of protrusive force. The membrane tension force is computed using
355 the functional derivative *Camley et al.* (*2014*) $F_{mem} = \frac{\delta H_{tension}(\phi)}{\delta\phi}\nabla\phi/\delta_\epsilon$, with $\delta_\epsilon = \epsilon|\nabla\phi|^2$ and

$$H_{tension}(\phi) = \gamma \int (\frac{\epsilon}{2}|\nabla\phi|^2 + \frac{G(\phi)}{\epsilon})d^2\boldsymbol{r}. \tag{5}$$

Here, $G(\phi)$ is a double well potential with minima at $\phi = 1$ and $\phi = 0$: $G(\phi) = 18\phi^2(1-\phi)^2$. As in our
earlier work *Camley et al.* (*2017*) we neglect membrane bending and we have verified that it does
not qualitatively change the results. We implement area conservation as $F_{area} = B_S(\int \phi d^2\boldsymbol{r} - S_0)\hat{n}$
where $B_S$ represents the strength of the area conservation and $S_0$ is the prescribed area size
determined by initial cell radius $r$ through $S_0 = \pi r^2$. The friction is $F_{fric} = \xi\boldsymbol{v}$ so that $\boldsymbol{v}$ is obtained
from the force balance equation: $\boldsymbol{v} = (F_{act} + F_{mem} + F_{area})/\xi$. Note that the friction coefficient takes
into account the interaction with the substrate, and that fluid drag can be ignored *Del Alamo et al.*
(*2007*). The motion of the phase field $\phi$ is then determined by the advective equation $\partial\phi/\partial t = -\boldsymbol{v}\cdot\nabla\phi$.
Finally, coupling the phase field equations to the reaction-diffusion equations presented in the
main text, we arrive at the full equations:

$$\frac{\partial(\phi A)}{\partial t} = D_A\nabla\cdot(\phi\nabla A) + \phi[(\frac{k_a A^2}{K_a^2 + A^2} + b)(A_t - A) - (d_1 + d_2 R)A + \zeta_1(t)], \tag{6}$$

$$\frac{\partial(\phi R)}{\partial t} = D_R\nabla\cdot(\phi\nabla R) + \phi[\frac{c_2 A - c_1 R}{\tau} + \zeta_2(t)], \tag{7}$$

$$\xi\frac{\partial\phi}{\partial t} = \eta M(A)|\nabla\phi| + \gamma(\nabla^2\phi - \frac{G'(\phi)}{\epsilon^2}) - B_S(\int \phi d^2\boldsymbol{r} - S_0)|\nabla\phi|. \tag{8}$$

356 Through the coupling of $\phi$ to the reaction-diffusion equations, all reaction and diffusion processes
357 are constrained to be inside the auxiliary field *Kockelkoren et al.* (*2003*). The membrane tension
358 parameter is similar to the one used in earlier studies *Shao et al.* (*2010*, 2012); *Camley et al.* (*2014*)
359 and taken from *Simson et al.* (*1998*). The parameters of the biochemical module are estimated
360 from experiments *Arai et al.* (*2010*); *Gerhardt et al.* (*2014*), such that the minimum wave speed in
361 simulations is approximately $0.12\mu$m/s and the wavelength is about $15\mu$m. Note, however, that we
362 can rescale time constants to make simulations more efficient. Therefore, these values are obtained
363 after increasing $\tau$ and time by a factor of 2 and 5, respectively.

## Numerical details

365 The parameters used for numerical simulations are listed in Table 1. Equations are evolved in a
366 region with size of $L_x \times L_y$=50$\times$50 $\mu$m with discrete grids of n$\times$m=256$\times$256 and periodic boundary
367 conditions are used. Eq.8 is discretized using the forward Euler method with $\partial_t\phi = (\phi^{(n+1)} - \phi^{(n)})/\Delta t$.
368 Derivatives are calculated using finite difference formulas: $\partial_x\phi = (\phi_{i+1,j} - \phi_{i-1,j})/(2\Delta x)$ and $\partial_x^2\phi =$
369 $(\phi_{i+1,j} + \phi_{i-1,j} - 2\phi_{i,j})/\Delta x^2$, with similar equations for the derivatives in the $y$-direction. Eq.6&7 are
370 discretized using the forward Euler scheme with $\partial_t(\phi A) = \phi^{(n)}(A^{(n+1)} - A^{(n)})/\Delta t + A^{(n)}(\phi^{(n+1)} - \phi^{(n)})/\Delta t$.
371 The diffusion terms $\nabla \cdot (\phi \nabla A)$ are also approximated using finite difference. The $x$-term, for example,
372 reads $[(\phi_{i+1,j} + \phi_{i,j})(A_{i+1,j} - A_{i,j})/(2\Delta x) - (\phi_{i,j} + \phi_{i-1,j})(A_{i,j} - A_{i-1,j})/(2\Delta x)]/\Delta x$. The white noise terms
373 are simulated as Wiener processes with $\zeta(t)\Delta t = \sqrt{\sigma \Delta t} N(0,1)$. As initial condition for $\phi$, we use a
374 disk $\phi = \frac{1}{2}[1 + \tanh(3(r - r_0)/\epsilon)]$, where $r_0$ is the prescribed radius and $A = R = 0$. The activator and
375 inhibitor concentration outside the boundary is 0. To implement this boundary condition, we solve
376 Eq.6&7 only in region $\epsilon_0$ away from $\phi = 1/2$ which is $\phi > \chi = 1/2 + 1/2\tanh(-3\epsilon_0/\epsilon) \approx 0.0025$, and
377 leave $A = R = 0$ outside this region. Here, we have taken $\epsilon_0 = 2\mu$m.

378 Equations are parallelized with CUDA and simulated using GPUs. Typical simulations speeds on
379 a high-end graphics board are less than one minute for 100s of model time.

## Identification of migration modes

381 In our simulations, we track the motion of the center of mass of the cell which results in a cell
382 trajectory. Oscillatory cells are defined as cells with a vanishing center of mass speed (see also
383 Fig. 2c). To distinguish amoeboid-like from keratocyte-like cells we can use one of two strategies.
384 The first one is identical to the one used in the experiments and uses the position of the center
385 of mass at discrete time intervals. We then compute the angle between the vector connecting
386 consecutive points and an arbitrary fixed axis and compute the standard deviation of this distribu-
387 tion. Keratocyte-like cells, which move more persistently and thus have straighter trajectories, will
388 have a smaller standard deviation than amoeboid-like cells (Fig. 2b). The result is shown in Fig. 2e
389 where we plot the standard deviation for 100 consecutive intervals, separated by 3s as a function of
390 protrusion strength (blue curve). Alternatively, taking advantage of the high temporal resolution of
391 the computational tracks, we can use the curvature of the cell trajectory to identify the transition
392 between amoeboid-like and keratocyte-like cells. This is also shown in Fig. 2e where we plot the
393 average curvature $\langle \kappa \rangle = \int \kappa(l)dl/L$ (red curve) as a function of protrusion strength. Here, $\kappa(l)$ is the
394 local curvature, and $L$ is the total length of the trajectory. We can then define keratocyte-like cells
395 as those cells with a standard deviation smaller than 2° or with an average curvature smaller than
396 0.02 $\mu m^{-1}$.

397 To identify the migration mode in the experiments we also track the centroid of the cell. However,
398 since the temporal resolution in the experiments are much lower than that of our simulations, we
399 cannot employ the average curvature identification described above. Instead, we use the angle
400 method and compute angles between two successive positions, separated by 30s. The standard
401 deviation of this angle is then computed for 5 consecutive pairs and keratocyte-like cells are defined
402 by having a standard deviation less than 25°. To determine whether cells can be considered
403 oscillatory we compute the cell area and evaluate three criteria. First, we compute the coefficient of
404 variation COV (ratio of the standard deviation and the mean) of the area oscillations (computed

405    using 5 consecutive frames separated by 30 s). Second, we determine the maximum (peaks) and
406    minimum values (valleys) in a time trace of the cell area (see Fig. 3e) and quantify the ratio of the
407    difference between the average peak and valley and the average peak: P=(<peak>-<valley>)/<peak>.
408    Third, we evaluate the total amount of time $T_{tot}$ an oscillation is present. Oscillatory cells are then
409    defined as cells with COV>5%, P>19%, and $T_{tot}$>40 min.

## Speed of keratocyte-like cells

411    The local cell boundary velocity can be approximated as $\boldsymbol{v} = \hat{\boldsymbol{n}}\eta M(A)/\xi$. Since, for keratocyte-like
412    cells, the front is almost flat (see main text Fig.2), the cell speed can be approximated as $v = \alpha\eta/\xi$,
413    where $\alpha$ is the average of $M(A)$ across the boundary: $\alpha = \int_{-\epsilon}^{\epsilon} M(A)\phi dx/(2\epsilon) \approx 0.55$. Thus, the speed
414    of keratocyte-like cells only depends on the protrusive force and the friction but not on the tension
415    or on the inhibitor timescale. We can verify this in simulations by changing the tension $\gamma$ and the
416    inhibitor's timescale $\tau$ while keeping other parameters fixed. The results are shown in Fig2–Figure
417    Supplement 1 which demonstrates that the cell speed changes little if these parameters are varied.

## Traveling waves

419    Our relaxation oscillator system exhibits traveling waves with a minimum speed that depends
420    on the timescale of the inhibitor and its diffusion constant. Our model can be written as $\partial_t A =$
421    $D\nabla^2 A + f(A, R)$, $\partial_t R = D\nabla^2 R + g(A, R)$, where $f(A, R)$ and $g(A, R)$ can be found from Eq.6&7. First we
422    consider the case of $\tau \to \infty$ and $D_R = 0$ so that the inhibitor is uniformly distributed and constant:
423    $R = R_0$. The relevant equation now is $\partial_t A = D\partial_x^2 A + f(A; R_0)$. When $R_0$ is in a proper range, there are
424    three steady states $A = A_{1,2,3}$, with $A_1 < A_2 < A_3$ and $A = A_{1,3}$ stable and $A = A_2$ unstable. For a given
425    $R_0$, we seek for solutions of wave form $A(z) = A(x - ct)$. The excitable version of this system has been
426    extensively studied and for the cubic reaction term $k(u - u_1)(u_2 - u)(u - u_3)$ there is a stable traveling
427    wave solution that connects $u$ with $u_1$ and $u_3$ and has a wave speed $c = \sqrt{kD/2}(u_1 - 2u_2 + u_3)$ *Murray*
428    (*2002*). Likewise, our model $\partial_t A = D\partial_x^2 A + f(A; R_0)$, which has the same structure as the excitable
429    system with a cubic reaction equation, has a stable traveling wave with speed $c \approx w(A_1 - 2A_2 + A_3)$
430    which depends on $R_0$ through $A_{1,2,3}$. Here, $w$ is a constant that only depends on the diffusion
431    coefficient $D_A$ and reaction rates (cf. $\sqrt{kD/2}$ for the cubic reaction equation).

432       For non-zero values of $\tau$ and $D_R$, the relaxation phase, characterized by the accumulation of
433    inhibitor, sets in behind the activator's wave front. From the above analysis, it can be deduced that
434    a necessary condition for a stable wave front is a constant profile of the inhibitor $R = R_0$ in the
435    width of the front. For $D_R = 0$, this can only be the case when $\tau$ is large so that the reaction rate of
436    the inhibitor is slow compared to the rate of the activator. Thus, there needs to be a separation of
437    timescales and the system has to obey relaxation dynamics. Furthermore, for $D_R > 0$, the activator
438    wave front is only stable if it can outrun the inhibitor's spreading speed which is proportional to
439    $\sqrt{D_R/\tau}$. Therefore, the traveling wave is only stable if both the reaction and diffusion of the inhibitor
440    are slow enough. In other words, stable waves will have a speed that exceeds a minimum value
441    which depends both on $D_R$ and $\tau$. In simulations, we can change $c_{\min}$ by changing the inhibitor's
442    diffusion coefficient $D_R$ and the timescale $\tau$. As expected, larger $D_R$ and smaller $\tau$ leads to larger
443    $c_{\min}$, and consequently larger $\eta_{c,1}$ (Fig2–Figure Supplement 2a&b).

## The role of tension in morphology

445    Tension is important to maintain the unidirectional movement of keratocyte-like cells. In our model,
446    at the two lateral ends of the traveling wave the morphology is determined by a balance between
447    the protrusive force and the tension which is determined by the local curvature and the parameter
448    $\gamma$. When the protrusive force increases, a larger membrane curvature is necessary to balance the
449    protrusive force, resulting in a flatter front and a decreased front-back distance. If $\gamma$ is not large
450    enough, the traveling wavefront can have a turning instability: the cell will no longer migrate along
451    a straight path and will make a turn *Camley et al.* (*2017*). An example of this instability and the
452    resulting motion is shown in Fig2–Figure Supplement 3 a where we decrease the surface tension

453  by a factor of 2 (from $\gamma$=2pN/$\mu$m to $\gamma$=1pN/$\mu$m). Similar to *Camley et al.* (*2017*), the cell can also be
454  destabilized by increasing the diffusion of the activator and inhibitor. An example of a simulation
455  showing this can be found in Fig2–Figure Supplement 3 b.

### Parameter variations

457  We have examined how the model results change when certain parameters are varied. For example,
458  we can extend the $(\eta, r)$ phase space to larger values of $r$ as shown in Fig2–Figure Supplement 4
459  a. For cell sizes that are beyond ones observed in experiments, we find that the critical protrusive
460  force $\eta_{c,2}$ saturates. For these large values of $r$, a dominant wave forms at the front of the cell and
461  new waves that are generated at the back of the cell are not strong enough to break this dominant
462  wave's persistency. The cell will move persistently in the direction of the dominant wave, with
463  smaller waves repeatedly appearing at the back, as shown in the snapshot presented in Fig2–Figure
464  Supplement 4 a. For keratocyte-like cells with a single wave, $d$ will saturate to the wavelength
465  $\lambda \approx 13\mu$m, as shown in Fig2–Figure Supplement 4 b. Finally, we have verified that changing the Hill
466  coefficient in $M(A)$ does not change the phase diagram and thus the transitions in a qualitative
467  fashion. This is shown in Fig2–Figure Supplement 4 c where we plot the boundaries between the
468  different migration modes in the phase diagram for three different values of the Hill coefficient.

### Varying area conservation

470  Real cells are three-dimensional objects in which the changing of the basal surface area will be
471  compensated by the morphological changes away from the substrate. Our model represents the
472  cell as a two-dimensional object and therefore includes an area conservation term. Making the
473  strength of this area conversation large in simulations allows us to define and sample the $(\eta, r)$
474  phase space (Fig. 2b). To determine how this area conservation term affects the observed dynamics,
475  we reduce the area conservation parameter from $S_B = 10$ to $S_B = 0.1$. As shown in Fig2–Figure
476  Supplement 5, all migration modes are still present. For small values of $\eta$, cells are oscillatory and,
477  compared to large values of $S_B$, exhibit measurable oscillations in cell size (Fig2–Figure Supplement
478  5 a-c). Furthermore, increasing the value of the protrusive strengths results in amoeboid-like motion
479  while even larger values of $\eta$ lead to keratocyte-like cells (Fig2–Figure Supplement 5 d).

### Excitable model

481  Our biochemical model is based on relaxation oscillation dynamics. However, it is straightforward
482  to consider an excitable version of the model. For this, we take $c_2 = 30, \sigma = 0.1\mu M^2 \mu m^2/s$ and keep
483  all the other parameters same as listed in Table S1. For the excitable version of our biochemical
484  module, we find similar migration mode transitions as found in the main text as well as a qualitatively
485  similar phase diagram (Fig2–Figure Supplement 6 a and b). Specifically, we also find a nonmotile,
486  amoeboid-like, and a keratocyte-like mode (Fig2–Figure Supplement 6 a). In the excitable case,
487  however, perturbations are required to initiate waves and movement. As a consequence, the
488  patterns of activator are more noisy than for the oscillation model and the non-motile cells do not
489  exhibit oscillatory dynamics. Finally, the transition between nonmotile cells and amoeboid-like cells
490  is also subcritical (Fig2–Figure Supplement 6 c).

### Experiments

492  Wild-type AX2 cells were transformed with the plasmid expressing limE-delta-coil-GFP. Cells were
493  kept in exponential growth phase in a shaker at 22°C in HL5 media with hygromycin (50$\mu$g/mL). On
494  the day before the experiment, cells were diluted to low concentration (1-2$\times10^5$ cells/mL) to stop
495  the exponential growth. After 15h-18h, cell concentration reached 2-5$\times10^5$ cells/mL and $10^5$ cells
496  were plated in a 50mm round chamber with glass bottom (WillCo). After 15min, cells attached to
497  the substrate and HL5 was replaced with 7mL DB (5 mM Na$_2$HPO$_4$, 5 mM KH$_2$PO$_4$,200$\mu$M CaCl$_2$, 2
498  mM MgCl$_2$, pH6.5). Specified amount was diluted in 500$\mu$L of DB and added to the sample using a
499  pipette at 6h of starvation.

Differential interference contrast (DIC) images are taken every 30s in six fields of view across the sample using a 10x objective from 5h45 to 6h30 after beginning of starvation. Cell centroids, area, minor and major axis are tracked using Slidebook 6 (Intelligent Imaging Innovations). Statistical analysis of trajectories is performed in MATLAB (2018a; The Mathworks). Experimental data presented before latrunculin B are for cells between 5h45 to 6h of starvation, whereas effect of the drug is quantified on cells from 6h15 to 6h30. Speeds are measured using a time interval of 1min. For each concentration, data are collected on three different days, resulting in N=333 , N=315, N=385, N=567, and N=399 for 0, 1, 2, 3, and 4 nM latruculin, respectively. P values are computed with the Wilcoxon rank sum test. Fluorescent images (488-nm excitation) are captured with a 63x oil objective using a spinning-disk confocal Zeiss Axio Observer inverted microscope equipped with a Roper Quantum 512SC cameras.

**Videos**

Video 1: simulation results for $r = 8\mu$m and $\eta = 2$ pN. Video 2: simulation results for $r = 8\mu$m and $\eta = 4$ pN. Video 3: simulation results for $r = 8\mu$m and $\eta = 11$ pN. Video 4: experimental results with $2\mu$M Latrunculin B added at time 1h45min.

**References**

**Allard J**, Mogilner A. Traveling waves in actin dynamics and cell motility. Current opinion in cell biology. 2013; 25(1):107–115.

**Arai Y**, Shibata T, Matsuoka S, Sato MJ, Yanagida T, Ueda M. Self-organization of the phosphatidylinositol lipids signaling system for random cell migration. Proceedings of the National Academy of Sciences. 2010; 107(27):12399–12404.

**Asano Y**, Mizuno T, Kon T, Nagasaki A, Sutoh K, Uyeda TQ. Keratocyte-like locomotion in amiB-null Dictyostelium cells. Cell motility and the cytoskeleton. 2004; 59(1):17–27.

**Barnhart EL**, Allard J, Lou SS, Theriot JA, Mogilner A. Adhesion-dependent wave generation in crawling cells. Current Biology. 2017; 27(1):27–38.

**Bergert M**, Chandradoss SD, Desai RA, Paluch E. Cell mechanics control rapid transitions between blebs and lamellipodia during migration. Proc Natl Acad Sci USA. 2012; 109(36):14434–14439.

**Beta C**, Amselem G, Bodenschatz E. A bistable mechanism for directional sensing. New Journal of Physics. 2008; 10(8):083015.

**Camley BA**, Zhang Y, Zhao Y, Li B, Ben-Jacob E, Levine H, Rappel WJ. Polarity mechanisms such as contact inhibition of locomotion regulate persistent rotational motion of mammalian cells on micropatterns. Proc Natl Acad Sci U S A. 2014; 111(41):14770–14775.

**Camley BA**, Zhao Y, Li B, Levine H, Rappel WJ. Periodic migration in a physical model of cells on micropatterns. Physical Review Letters. 2013; 111(15):158102.

**Camley BA**, Zhao Y, Li B, Levine H, Rappel WJ. Crawling and turning in a minimal reaction-diffusion cell motility model: coupling cell shape and biochemistry. Physical Review E. 2017; 95(1):012401.

**Cao Y**, Karmakar R, Ghabache E, Gutierrez E, Zhao Y, Groisman A, Levine H, Camley BA, Rappel WJ. Cell motility dependence on adhesive wetting. Soft Matter. 2019; 15:2043–2050. doi: 10.1039/C8SM01832D.

**Case LB**, Waterman CM. Adhesive F-actin waves: a novel integrin-mediated adhesion complex coupled to ventral actin polymerization. PloS one. 2011; 6(11):e26631.

**Charras G**, Sahai E. Physical influences of the extracellular environment on cell migration. Nature reviews Molecular cell biology. 2014; 15(12):813.

**Csikász-Nagy A**, Győrffy B, Alt W, Tyson JJ, Novák B. Spatial controls for growth zone formation during the fission yeast cell cycle. Yeast. 2008; 25(1):59–69.

**Del Alamo JC**, Meili R, Alonso-Latorre B, Rodríguez-Rodríguez J, Aliseda A, Firtel RA, Lasheras JC. Spatio-temporal analysis of eukaryotic cell motility by improved force cytometry. Proceedings of the National Academy of Sciences. 2007; 104(33):13343–13348.

547  **Friedl P**, Alexander S. Cancer invasion and the microenvironment: plasticity and reciprocity. Cell. 2011;
548      147(5):992–1009.

549  **Fukushima S**, Matsuoka S, Ueda M. Excitable dynamics of Ras triggers self-organized PIP3 signaling for
550      spontaneous cell migration. bioRxiv. 2018; p. 356105.

551  **Gerhardt M**, Ecke M, Walz M, Stengl A, Beta C, Gerisch G. Actin and PIP3 waves in giant cells reveal the inherent
552      length scale of an excited state. J Cell Sci. 2014; 127(20):4507–4517.

553  **Gerisch G**, Schroth-Diez B, Müller-Taubenberger A, Ecke M. PIP3 waves and PTEN dynamics in the emergence of
554      cell polarity. Biophysical journal. 2012; 103(6):1170–1178.

555  **Goldstein B**, Macara IG. The PAR proteins: fundamental players in animal cell polarization. Developmental cell.
556      2007; 13(5):609–622.

557  **Jilkine A**, Edelstein-Keshet L. A comparison of mathematical models for polarization of single eukaryotic cells in
558      response to guided cues. PLoS computational biology. 2011; 7(4):e1001121.

559  **Keener JP**. Waves in excitable media. SIAM Journal on Applied Mathematics. 1980; 39(3):528–548.

560  **Keren K**, Pincus Z, Allen GM, Barnhart EL, Marriott G, Mogilner A, Theriot JA. Mechanism of shape determination
561      in motile cells. Nature. 2008; 453(7194):475–480.

562  **Knoch F**, Tarantola M, Bodenschatz E, Rappel WJ. Modeling self-organized spatio-temporal patterns of PIP3 and
563      PTEN during spontaneous cell polarization. Physical biology. 2014; 11(4):046002.

564  **Kockelkoren J**, Levine H, Rappel WJ. Computational approach for modeling intra-and extracellular dynamics.
565      Physical Review E. 2003; 68(3):037702.

566  **Kopell N**, Howard LN. Plane wave solutions to reaction-diffusion equations. Studies in Applied Mathematics.
567      1973; 52(4):291–328.

568  **Liu YJ**, Le Berre M, Lautenschlaeger F, Maiuri P, Callan-Jones A, Heuzé M, Takaki T, Voituriez R, Piel M. Confinement
569      and low adhesion induce fast amoeboid migration of slow mesenchymal cells. Cell. 2015; 160(4):659–672.

570  **Marth W**, Voigt A. Signaling networks and cell motility: a computational approach using a phase field description.
571      Journal of mathematical biology. 2014; 69(1):91–112.

572  **Matsuoka S**, Ueda M. Mutual inhibition between PTEN and PIP3 generates bistability for polarity in motile cells.
573      Nature communications. 2018; 9(1):4481.

574  **Meinhardt H**. Orientation of chemotactic cells and growth cones: models and mechanisms. J Cell Sci. 1999;
575      112(17):2867–2874.

576  **Miao Y**, Bhattacharya S, Banerjee T, Abubaker-Sharif B, Long Y, Inoue T, Iglesias PA, Devreotes PN. Wave patterns
577      organize cellular protrusions and control cortical dynamics. Molecular systems biology. 2019; 15(3):e8585.

578  **Miao Y**, Bhattacharya S, Edwards M, Cai H, Inoue T, Iglesias PA, Devreotes PN. Altering the threshold of an
579      excitable signal transduction network changes cell migratory modes. Nature cell biology. 2017; 19(4):329.

580  **Montell DJ**. Border-cell migration: the race is on. Nature Reviews Molecular Cell Biology. 2003; 4(1):13–24.

581  **Mori Y**, Jilkine A, Edelstein-Keshet L. Wave-pinning and cell polarity from a bistable reaction-diffusion system.
582      Biophysical journal. 2008; 94(9):3684–3697.

583  **Murray JD**, Mathematical biology. Springer New York; 2002.

584  **Najem S**, Grant M. Phase-field approach to chemotactic driving of neutrophil morphodynamics. Physical Review
585      E. 2013; 88(3):034702.

586  **Nishimura SI**, Ueda M, Sasai M. Cortical factor feedback model for cellular locomotion and cytofission. PLoS
587      computational biology. 2009; 5(3):e1000310.

588  **Nishimura SI**, Ueda M, Sasai M. Non-Brownian dynamics and strategy of amoeboid cell locomotion. Physical
589      Review E. 2012; 85(4):041909.

590  **Otsuji M**, Ishihara S, Kaibuchi K, Mochizuki A, Kuroda S, et al. A mass conserved reaction–diffusion system
591      captures properties of cell polarity. PLoS computational biology. 2007; 3(6):e108.

**Park HO**, Bi E. Central roles of small GTPases in the development of cell polarity in yeast and beyond. Microbiol Mol Biol Rev. 2007; 71(1):48–96.

**Paul CD**, Mistriotis P, Konstantopoulos K. Cancer cell motility: lessons from migration in confined spaces. Nature Reviews Cancer. 2017; 17:131.

**Petrie RJ**, Yamada KM. Multiple mechanisms of 3D migration: the origins of plasticity. Current Opinion in Cell Biology. 2016; 42:7–12.

**Raftopoulou M**, Hall A. Cell migration: Rho GTPases lead the way. Developmental biology. 2004; 265(1):23–32.

**Rameh LE**, Cantley LC. The role of phosphoinositide 3-kinase lipid products in cell function. Journal of Biological Chemistry. 1999; 274(13):8347–8350.

**Rappel WJ**, Edelstein-Keshet L. Mechanisms of cell polarization. Current opinion in systems biology. 2017; 3:43–53.

**Ridley AJ**, Schwartz MA, Burridge K, Firtel RA, Ginsberg MH, Borisy G, Parsons JT, Horwitz AR. Cell migration: integrating signals from front to back. Science. 2003; 302(5651):1704–1709.

**Roussos ET**, Condeelis JS, Patsialou A. Chemotaxis in cancer. Nature Reviews Cancer. 2011; 11(8):573.

**Shao D**, Levine H, Rappel WJ. Coupling actin flow, adhesion, and morphology in a computational cell motility model. Proc Natl Acad Sci U S A. 2012; 109(18):6851–6856.

**Shao D**, Rappel WJ, Levine H. Computational model for cell morphodynamics. Physical Review Letters. 2010; 105(10):108104.

**Simson R**, Yang B, Moore SE, Doherty P, Walsh FS, Jacobson KA. Structural mosaicism on the submicron scale in the plasma membrane. Biophysical Journal. 1998; 74(1):297–308.

**Slaughter BD**, Smith SE, Li R. Symmetry breaking in the life cycle of the budding yeast. Cold Spring Harbor perspectives in biology. 2009; 1(3):a003384.

**Tanabe Y**, Kamimura Y, Ueda M. Parallel signaling pathways regulate excitable dynamics differently to mediate pseudopod formation during eukaryotic chemotaxis. J Cell Sci. 2018; 131(23):jcs214775.

**Vicker MG**. Eukaryotic cell locomotion depends on the propagation of self-organized reaction-diffusion waves and oscillations of actin filament assembly. Exp Cell Res. 2002 Apr; 275(1):54–66.

**Webb DJ**, Horwitz AF. New dimensions in cell migration. Nature Cell Biology. 2003; 5(8):690.

**Weiner OD**, Marganski WA, Wu LF, Altschuler SJ, Kirschner MW. An actin-based wave generator organizes cell motility. PLoS biology. 2007; 5(9):e221.

**Whitelam S**, Bretschneider T, Burroughs NJ. Transformation from spots to waves in a model of actin pattern formation. Physical review letters. 2009; 102(19):198103.

**Xiong Y**, Huang CH, Iglesias PA, Devreotes PN. Cells navigate with a local-excitation, global-inhibition-biased excitable network. Proceedings of the National Academy of Sciences. 2010; .

**Ziebert F**, Swaminathan S, Aranson IS. Model for self-polarization and motility of keratocyte fragments. Journal of The Royal Society Interface. 2011; p. rsif20110433.

| Parameter | Description | Value |
|:---:|:---:|:---:|
| $\gamma$ | Tension | 2 pN $\mu$m |
| $\epsilon$ | Width of phase field | 2 $\mu$m |
| $B_S$ | Cell area conservation strength | 10 pN/$\mu m^2$ |
| $\xi$ | Friction coefficient | 10 pN s/$\mu m$ |
| $n$ | Hill coefficient of protrusive force | 3 |
| $k_a$ | Activation rate | 10 $s^{-1}$ |
| $K_a$ | Activation threshold | 1 $\mu$M |
| $b$ | Basal activation rate | 0.1 $s^{-1}$ |
| $A_t$ | Total activator concentration | 2 $\mu M$ |
| $d_1$ | Basal degradation rate | 1 $s^{-1}$ |
| $d_2$ | Degradation rate from inhibitor | 1 $\mu M^{-1} s^{-1}$ |
| $c_1$ | Inhibitor degradation coeffecient | 1 |
| $c_2$ | Inhibitor activation coefficient | 15 |
| $\tau$ | Time scale of negative feedback | 10 s |
| $D_A$ | Activator diffusion coefficient | 0.5 $\mu m^2/s$ |
| $D_R$ | Inhibitor diffusion coefficient | 0.5 $\mu m^2/s$ |
| $\sigma$ | Noise intensity | 0.01 $\mu M^2 \mu m^2/s$ |
| $\Delta t$ | Time step | 0.001 s |
| $n, m$ | Space grid size | 256,256 |
| $L_{x,y}$ | Space size | 50,50 $\mu$m |

**Table 1.** Model Parameters
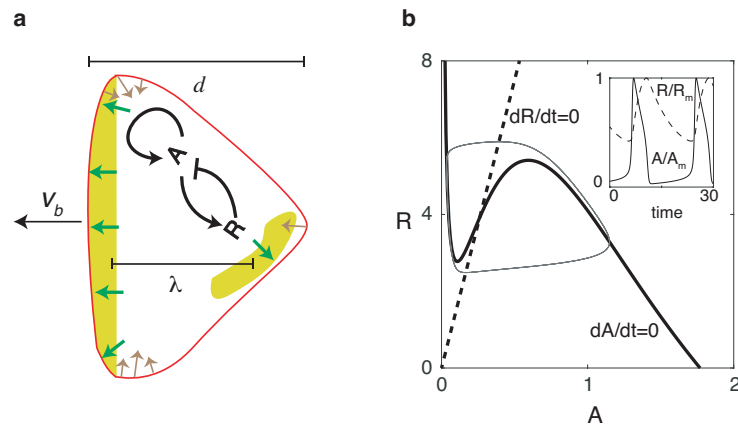
**Figure 1.** Reaction diffusion model coupled to a mechanical model. (a) Schematic illustration of the two-dimensional model: a self-activating activator field $A$, indicated in color, drives the movement of the cell membrane through protrusive forces that are normal to the membrane (green arrows). The membrane tension (denoted by brown arrows) is proportional to the local curvature while the cell also experiences a drag force that is proportional to the speed. One successive wave is generated behind the original one after a distance of $\lambda$. The cell's front-back distance is $d$, and the cell boundary is pushed outward with speed $v_b$. (b) Nullclines of the activator (solid line) and inhibitor (dashed line), along with the resulting trajectory in phase space (gray thin line). The inset shows the oscillations of $A$ and $R$, normalized by their maximum values $A_m$ and $R_m$.
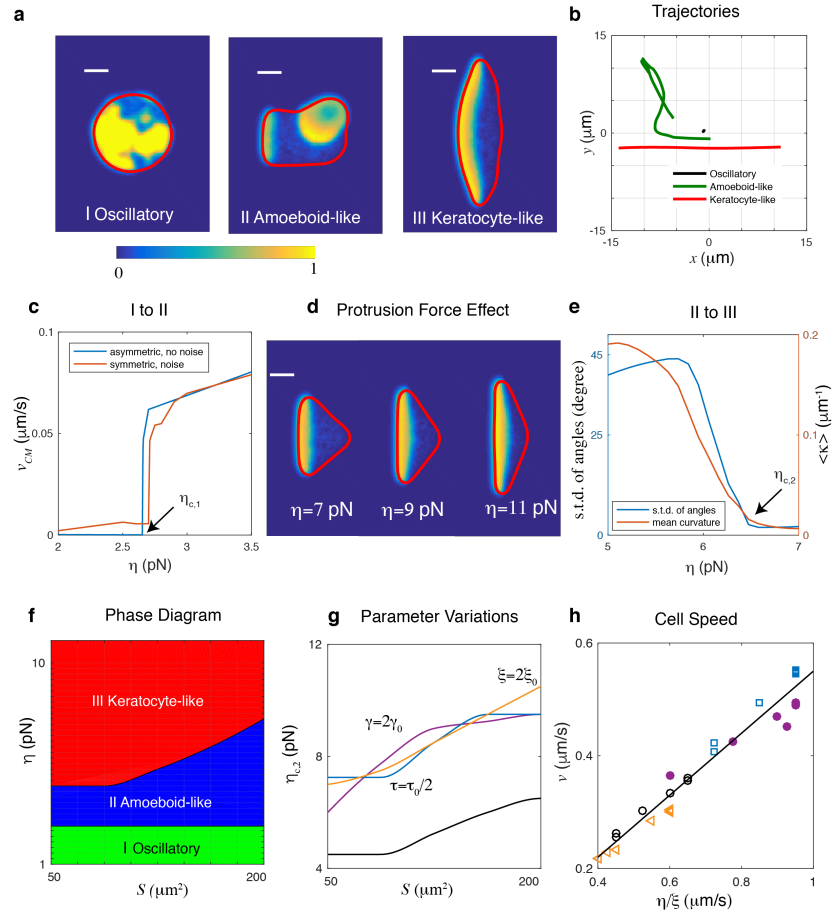
**Figure 2.** Different cell migration modes can be captured in the model by varying the protrusive strength $\eta$. (a) Snapshots of a simulated cell showing (I) an oscillatory cell ($\eta = 2$ pN), (II) an amoeboid-like cell ($\eta = 4$ pN), and (III) a keratocyte-like cell ($\eta = 11$ pN). All other parameters were assigned the default values and $r = 8\mu m$. Here, the activator concentration is shown using the color scale and the cell membrane is plotted as a red line (scale bar $5\mu m$). (b) The trajectories of the three cells in (a). (c) The transition from oscillatory cell to amoeboid-like cell, with speed of the center of mass of a cell as a function of protrusion strength $\eta$ for $r = 8\mu m$. The red curve represents results from initial conditions where noise is added to a homogeneous $A$ and $R$ field while the blue curve corresponds to simulations in which the initial activator is asymmetric. Cells become non-motile at a critical value of protrusion strength, $\eta_{c,1}$. (d) Increasing the protrusive force $\eta$ will result in flatter fronts in keratocyte-like cells and a decreased front-back distance. The simulations are carried out for fixed cell area $S$. (e) The transition from amoeboid-like cell to keratocyte-like cell quantified by either the average curvature along a trajectory or the standard deviation of the angles of trajectory points as a function of protrusion strength $\eta$ ($r = 8\mu m$). Cell moves unidirectionally when the protrusion strength $\eta > \eta_{c,2}$. (f) Phase diagram determined by systematically varying $\eta$ and the initial radius of the cell, $r$. Due to strong area conservation, cell area is determined through $S = \pi r^2$. (g) The transition line of amoeboid-like cell to keratocyte-like cell for different parameter values. (h) The speed of the keratocyte-like cell as a function of $\eta/\xi$. The black line is the predicted cell speed with $v_b = \alpha\eta/\xi$, where $\alpha \approx 0.55$. Symbols represent simulations using different parameter variations: empty circles, default parameters; triangles, $\xi = 2\xi_0$; filled circles, $\gamma = 2\gamma_0$; squares, $\tau = \tau_0/2$.

**Figure 2–Figure supplement 1.** Speed of keratocyte-like cells as a function of the surface tension and timescale of the inhibitor

**Figure 2–Figure supplement 2.** Critical protrusion strength $\eta_{c,1}$ as a function of the inhibitor's diffusion constant and time scale.

**Figure 2–Figure supplement 3.** Effects of tension

**Figure 2–Figure supplement 4.** Parameter variations in the model

**Figure 2–Figure supplement 5.** Oscillatory cells for strong and weak area conservation

**Figure 2–Figure supplement 6.** Excitable dynamics can reproduce identical qualitative results
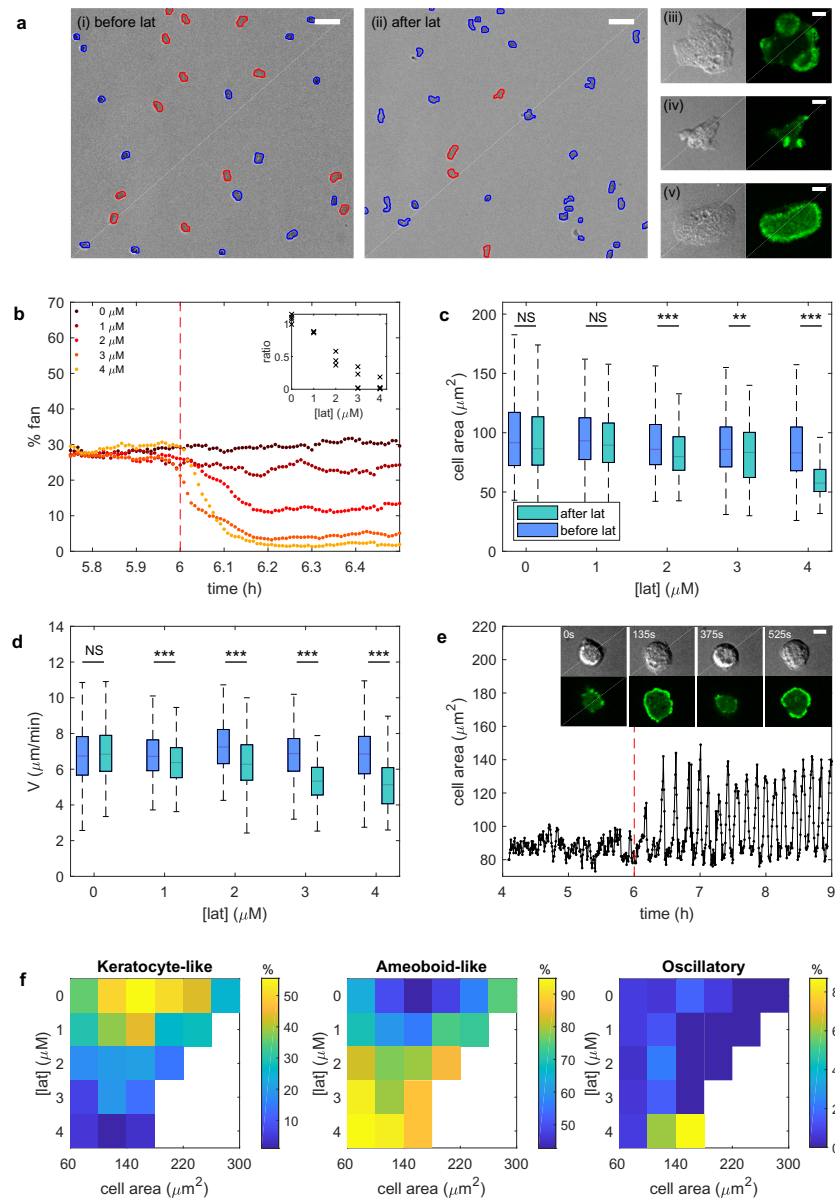
**Figure 3.** Experiments reveal different migration modes in Dictyostelium cells. (a) Snapshot of starved Dictyostelium cells before (left) and after (right) exposure to latrunculin B. Amoeboid-like cells are outlined in blue while keratocyte-like cells are outlined in red (scale bar: 50 $\mu$m). The panels on the right show high magnification views of amoeboid-like (top two) and keratocyte-like cells in which the freshly polymerized actin is visualized with limE-GFP (scale bar: 5 $\mu$m). (b) Percentage of keratocyte-like cells as a function of time for different concentrations of latrunculin B (introduced at 6 h, dashed line). Inset shows the ratio of keratocyte-like to all cells as a function of the latrunculin concentration for three repeats. (c) The cell area size of keratocyte-like cells before and after latrunculin exposure as a function of concentration. (d) The speed of keratocyte-like cells before and after latrunculin exposure as a function of concentration. (e) Basal cell area as a function of time for a cell that transitioned from amoeboid-like to oscillatory. Insets show snapshots of the cell at different time points (scale bar: 5 $\mu$m). (f) Percentage of cells in the keratocyte-like, amoeboid-like, and oscillatory mode of migration in the phase space spanned by cell area and latrunculin concentration. Percentage for each mode is visualized using the color bars. The number of cells for each data point varies between 7 and >1,000 and white corresponds to a data point with fewer than 7 total cells.

**Figure 3–Figure supplement 1.** The speed of amoeboid and keratocyte-like cells as a function of latrunculin concentration for different cell areas.

**Figure 3–Figure supplement 2.** The average period and coefficient of variation for area oscillations in oscillating cells after the exposure to latrunculin.
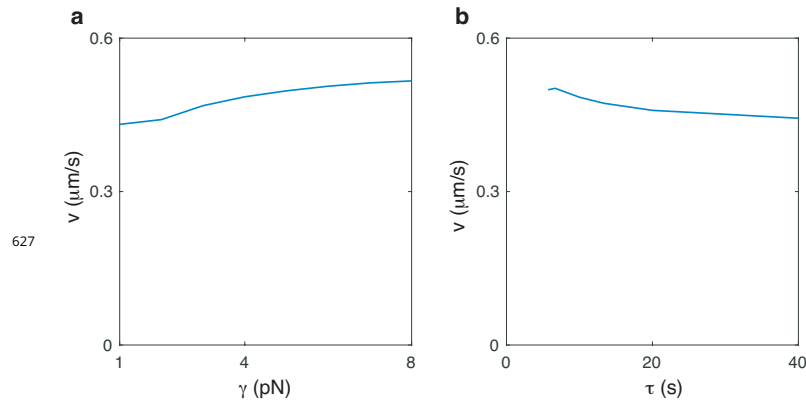
**Figure 2–Figure supplement 1.** Speed of keratocyte-like cells as a function of the surface tension (a) and the timescale of the inhibitor (b). Parameters are as in Table S1 with $r = 8\mu$m.

627



628
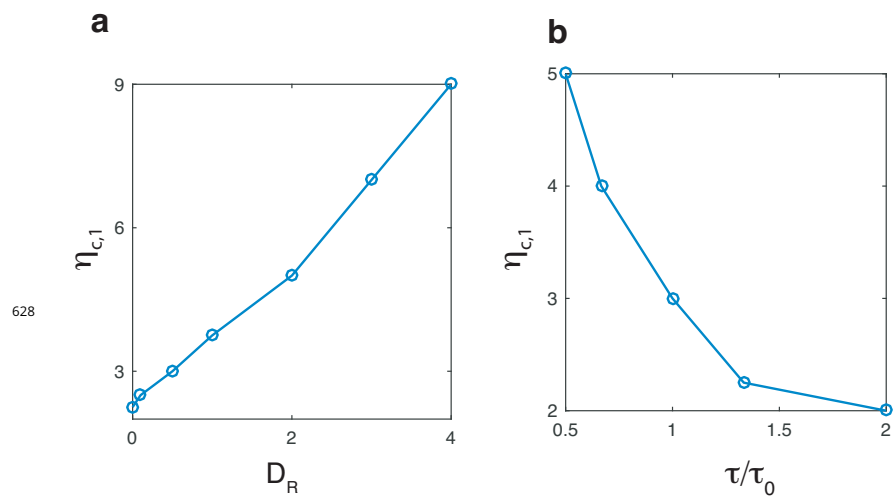
**Figure 2–Figure supplement 2.** (a) The critical value $\eta_{c,1}$ of protrusion strength as a function of inhibitor's diffusion constant $D_R$, and (b), the timescale of the inhibitor $\tau$, rescaled by the default value $\tau_0 = 10$s. Remaining parameters are as in Table S1 with $r = 8\mu$m.

**a**



**b**



629
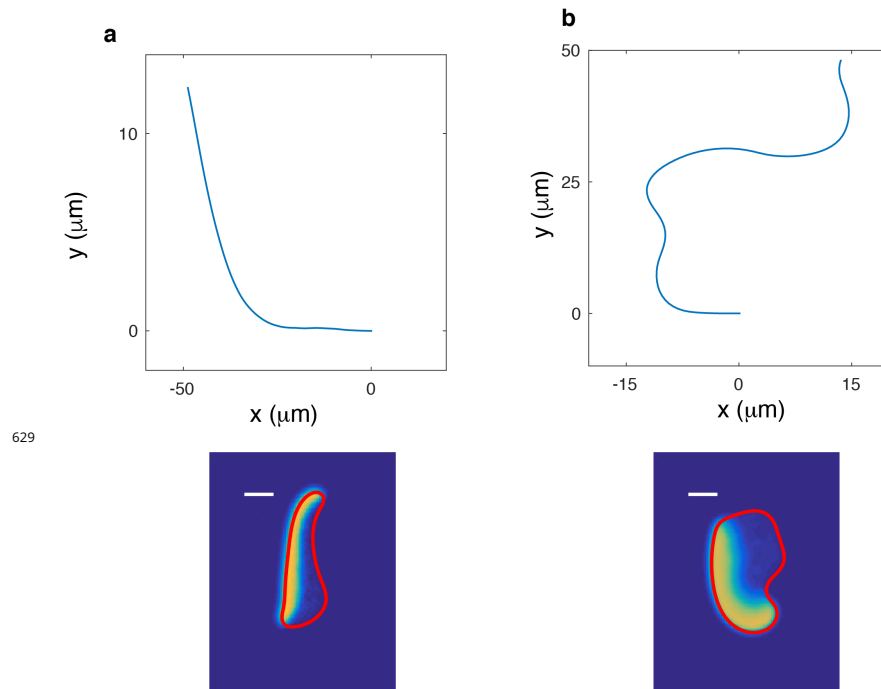
**Figure 2–Figure supplement 3.** Snapshot (bottom) and corresponding trajectory (top) of a cell that undergoes a turning instability. (a) Upon the reduction of surface tension from $\gamma$=2pN/$\mu$m to $\gamma$=1pN/$\mu$m. Parameters are taken from Table S1 with $r = 6\mu$m. (b) As in (a), but now after an increase in $D_A$ and $D_R$ to $D_A = D_R$=2 $\mu$m$^2$/s and $r = 8\mu$m.

**a**



**b**



630

**c**
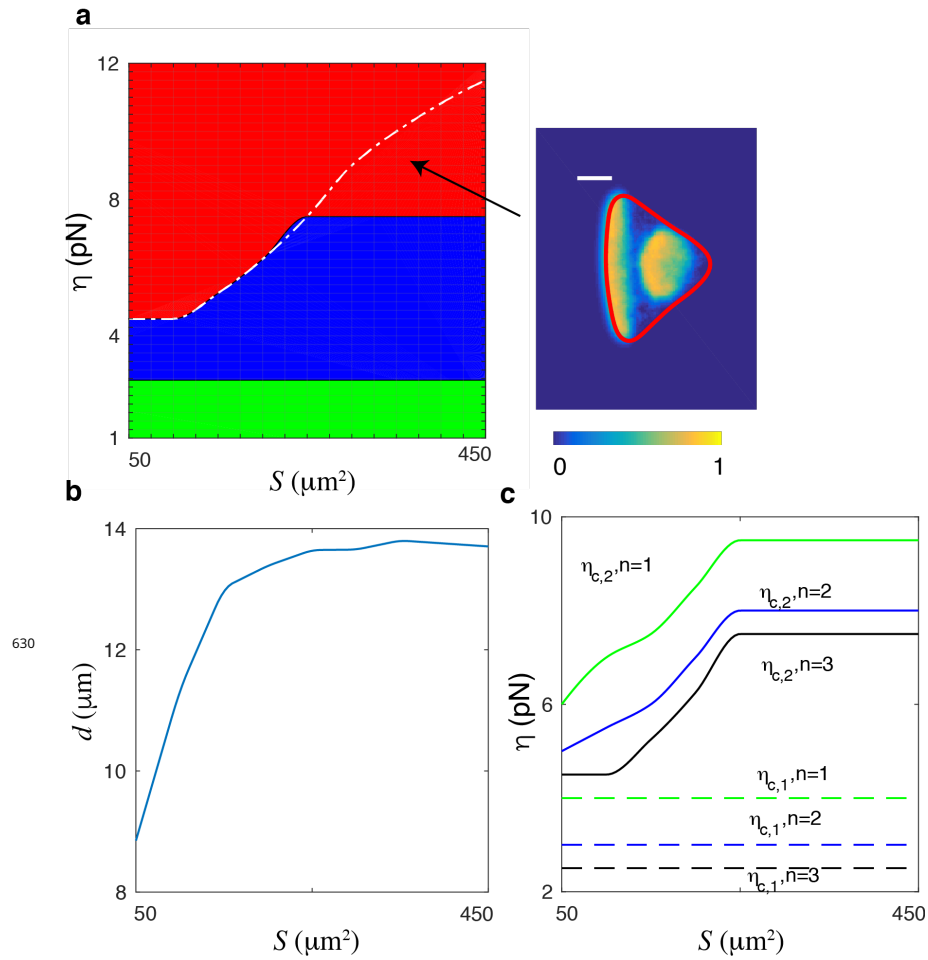


**Figure 2–Figure supplement 4.** Parameter variations in the model. (a) Phase space extended to maximum cell area $\sim 450\mu$m$^2$, corresponding to $r = 12\mu$m. Green: oscillatory cell; blue: amoeboid-like cell; red: keratocyte-like cell. The dashed white line corresponding to the separation line $d = \lambda$ above which the keratocyte-like cells exhibit a single wave and below which keratocyte-like cells move unidirectional but with small waves repeatedly appearing at the back of the cell. (b) The keratocyte-like cell's front-back distance $d$ along the white dashed line. The saturation value is the wavelength $\lambda \approx 13\mu$m. (c) Lines corresponding to $\eta_{c,1}$ and $\eta_{c,2}$ in the $(\eta, S)$ phase space for different values of the Hill coefficient $n$. For all values of $n$ used in the simulations, $\eta_{c,1}$ is independent of the cell radius $r$ while $\eta_{c,2}$ increases with $r$, and thus $S$, and eventually saturates.

631
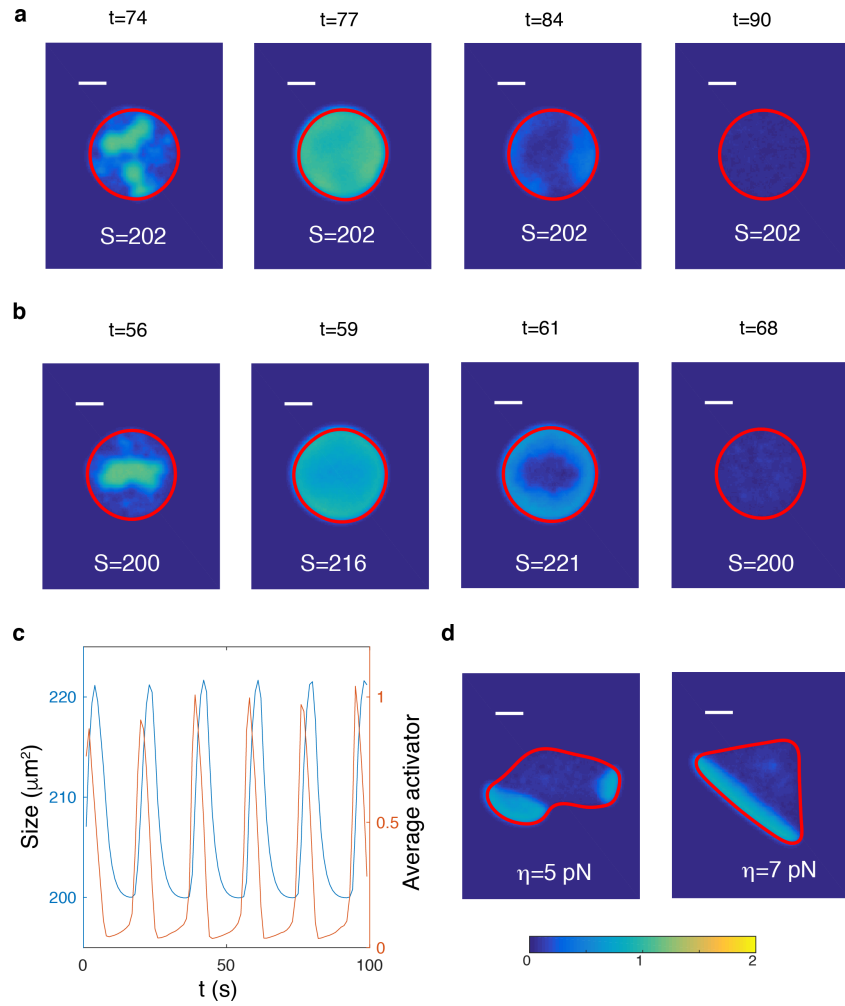
**Figure 2–Figure supplement 5.** Oscillatory cells for strong (a, $B_S = 10$) and weak (b, $B_S = 0.1$) area conservation. Parameters are as in Table 1 with $\eta = 2.5$ and $r = 8\mu$m. (c) Cell size (blue) and average activator concentration (red) as a function of time for the oscillatory cell in panel b. (d) Left, example of amoeboid-like cell for weak area conservation ($B_S = 0.1$); right, example of keratocyte-like cell for weak area conservation ($B_S = 0.1$). The colors represent the activator concentration, as indicated by the color bar. Scalebar=5 $\mu$m.
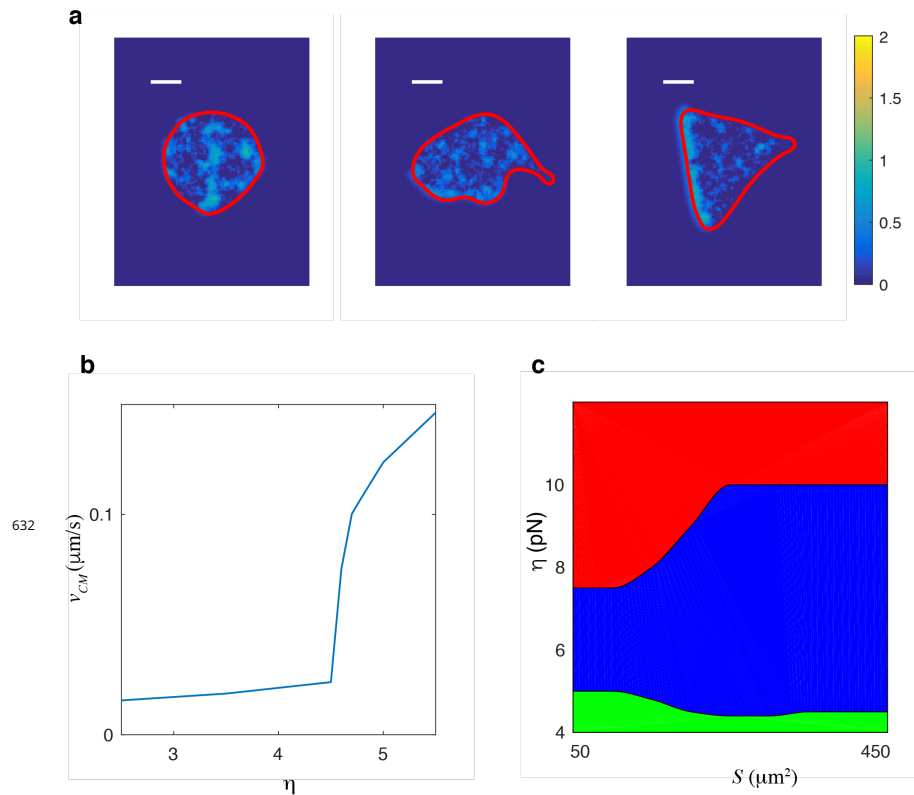
**Figure 2–Figure supplement 6.** Excitable dynamics can reproduce identical qualitative results. (a) Snapshots of the three different migration modes for an excitable version of the model. Left panel shows an nonmotile cell ($\eta = 2$), middle panel shows an amoeboid-like cell ($\eta = 4$), and the right panel displays a keratocyte-like cell ($\eta = 10$). (b) Speed of the center of mass as a function of critical protrusion strength. As for the relaxation oscillator model (Fig. 2c), the bifurcation is subcritical. (c) Phase diagram $(\eta, S)$ space with green corresponding to nonmotile cells, blue representing amoeboid-like cells, and red corresponding to keratocyte-like cells. Scalebar=5 $\mu$m.

632

633
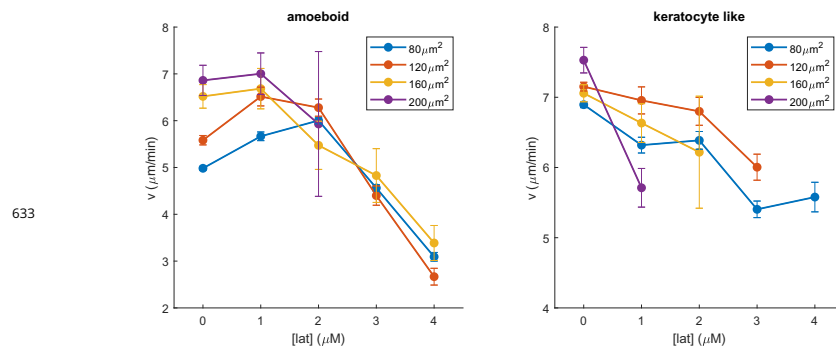


**Figure 3–Figure supplement 1.** Cell speed decreases as the latrunculin concentration increases. Cell areas were grouped in bins of 40 $\mu$m². Error bars represent the standard error of the mean.

634
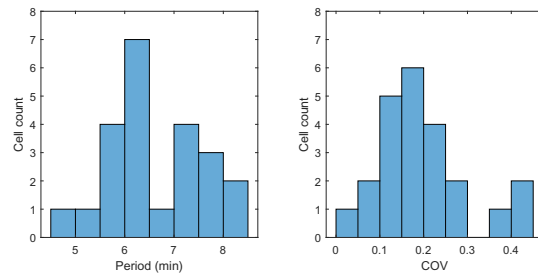


**Figure 3–Figure supplement 2.** The average period and coefficient of variation COV (ratio of the standard deviation and the mean) for area oscillations in oscillating cells after the exposure to $4\mu$M latrunculin (N=23).